Atmos. Chem. Phys. Discuss., 15, 21539–21582, 2015
www.atmos-chem-phys-discuss.net/15/21539/2015/
doi:10.5194/acpd-15-21539-2015

Atmospheric Chemistry and Physics Discussions

Influence of biomass burning on CCN number and hygroscopicity during summertime in the eastern Mediterranean

A. Bougiatioti[1,2,3], S. Bezantakos[4,5], I. Stavroulas[3], N. Kalivitis[3], P. Kokkalis[2], G. Biskos[6,7], N. Mihalopoulos[3,7,10], A. Papayannis[2], and A. Nenes[1,8,9]

[1]School of Earth and Atmospheric Sciences, Georgia Institute of Technology, Atlanta, GA, USA
[2]Laser Remote Sensing Unit, National Technical University of Athens, Zografou, Athens, Greece
[3]ECPL, Department of Chemistry, University of Crete, Voutes, 71003 Heraklion, Greece
[4]Department of Environment, University of the Aegean, Mytilene, 81100, Greece
[5]Institute of Nuclear Technology and Radiation Protection, NCSR "Demokritos", 15310 Ag. Paraskevi, Athens, Greece
[6]Faculty of Civil Engineering and Geosciences, Delft University of Technology, Delft 2728 CN, the Netherlands
[7]Energy Environment and Water Research Center, The Cyprus Institute, Nicosia 2121, Cyprus
[8]School of Chemical and Biomolecular Engineering, Georgia Institute of Technology, Atlanta, GA, USA
[9]Institute of Chemical Engineering Sciences (ICE-HT), FORTH, Patras, Greece

[10]IERSD, National Observatory of Athens, P. Penteli 15236, Athens, Greece

Received: 14 July 2015 – Accepted: 20 July 2015 – Published: 10 August 2015

Correspondence to: A. Bougiatioti (kbougiatioti@gmail.com)

Published by Copernicus Publications on behalf of the European Geosciences Union.

ACPD
15, 21539–21582, 2015

Abstract

This study investigates the CCN activity and hygroscopic properties of particles influenced by biomass burning in the eastern Mediterranean. Air masses sampled were subject to a range of atmospheric processing (several hours up to 3 days). Values of the hygroscopicity parameter, κ, were derived from cloud condensation nuclei (CCN) measurements and a Hygroscopic Tandem Differential Mobility Analyzer (HTDMA). An Aerosol Chemical Speciation Monitor (ACSM) was also used to determine the chemical composition and mass concentration of non-refractory components of the submicron aerosol fraction. During fire events, the increased organic content (and lower inorganic fraction) of the aerosol decreases the hygroscopicity parameter, κ, for all particle sizes. The reason, however, for this decrease was not the same for all size modes; smaller particle sizes appeared to be richer in less hygroscopic, less CCN-active components due to coagulation processes while larger particles become less hygroscopic during the biomass burning events due to condensation of less hygroscopic gaseous compounds. In addition, smaller particles exhibited considerable chemical dispersion (where hygroscopicity varied up to 100 % for particles of same size); larger particles, however, exhibited considerably less dispersion owing to the effects of aging and retained high levels of CCN activity. These conclusions are further supported by the observed mixing state determined by the HTDMA measurements. ACSM measurements indicate that the bulk composition reflects the hygroscopicity and chemical nature of the largest particles and a large fraction of the CCN concentrations sampled. Based on Positive Matrix Factorization (PMF) analysis of the organic ACSM spectra, CCN concentrations follow a similar trend with the BBOA component, with enhancements of CCN in biomass burning plumes ranging between 65 and 150 %, for supersaturations ranging between 0.2 and 0.7 %. Using multilinear regression, we determine the hygroscopicity of the prime organic aerosol components (BBOA, OOA-BB and OOA); it is found that the total organic hygroscopicity is very close to the inferred hygroscopicity of the oxygenated organic aerosol components. Finally, the transformation of freshly-

ACPD
15, 21539–21582, 2015

emitted biomass burning (BBOA) to more oxidized organic aerosol (OOA-BB) can result in a two-fold increase of the inferred organic hygroscopicity. Almost 10 % of the total aerosol hygroscopicity is related to the two biomass burning components (BBOA and OOA-BB), which in turn contribute almost 35 % to the fine-particle organic water of the aerosol. This is important as organic water can contribute to the atmospheric chemistry and the direct radiative forcing.

1 Introduction

Globally, biomass burning (BB) is a major source of atmospheric aerosols (Adreae et al., 2004). In the eastern Mediterranean, up to one third of the dry submicron aerosol mass during the summer period consists of highly oxidized organic compounds (Hildebrandt et al., 2010). During July–September, biomass-burning aerosol originates from long-range transport from Southern Europe and countries surrounding the Black Sea (Sciare et al., 2008). Bougiatioti et al. (2014) showed that of the total organic aerosol (OA), about 20 % is freshly-emitted biomass burning organic aerosol (BBOA), 30 % is oxidized, processed OA originating from BBOA (BB-OOA), and the remaining 50 % is highly oxidized aerosol that results from extensive atmospheric aging. Hence, in term of organic mass, during time periods of high biomass burning activity, up to 50 % of the aerosol can be influenced by these emissions.

Biomass burning aerosol particles have the potential to act as cloud condensation nuclei (CCN), thereby impact cloud properties and climate. Modeling studies suggest that BB is a significant global source of CCN number (Spracklen et al., 2011). It is therefore important to understand how biomass burning contributes to CCN and aerosol hygroscopicity and how it evolves in the atmosphere. Laboratory and field studies suggest that the water-soluble component of biomass burning aerosol is highly hygroscopic, about half of ammonium sulfate (Asa-Awuku et al., 2010; Cerully et al., 2014). Engelhart et al. (2012) found that freshly emitted BBOA displays a broad range of hygroscopicity (0.06 to 0.6) that considerably reduces after just a few hours of photochemical

ACPD
15, 21539–21582, 2015

processing, to a value of 0.2 ± 0.1. Few studies, however, focus on the hygroscopicity of ambient aerosol for a range of atmospheric aging.

In the current study we focus on the CCN activity and hygroscopicity of ambient aerosol influenced by biomass burning events in the eastern Mediterranean during summertime. The events were not local and air masses sampled were subject to a range of atmospheric processing (several hours up to 3 days). Smoke plumes sampled are identified by the Moderate Resolution Imaging Spectroradiometer (MODIS) (Remy and Kaiser, 2014) onboard the Terra and Aqua satellites and the laser remote sensing (lidar) system on board the space-borne Cloud-Aerosol Lidar with Orthogonal Polarization (CALIOP) platform (Winker et al., 2009; Mamouri et al., 2012). Values of the hygroscopicity parameter, κ, were derived from CCN and HTDMA measurements while the chemical composition and mass concentration of non-refractory components of the submicron aerosol fraction were studied using an Aerosol Chemical Speciation Monitor (ACSM). The originality of our study relies on the fact that, to our knowledge, very few field studies were able to focus on the hygroscopicity of ambient biomass burning aerosol for a range of atmospheric aging, which is addressed here. The study also examines the contribution of different organic aerosol components to the overall hygroscopicity which in turn may contribute to the aerosol liquid water content (LWC), as the potential of organic gases to partition to LWC is sometimes greater than the potential to partition to particle-phase organic matter (Carlton and Turpin, 2013). LWC is important as it has a direct effect on aerosol particles by enhancing scattering but also can contribute to the indirect effect by promoting secondary aerosol formation (Nguyen et al., 2013; Guo et al., 2015).

ACPD
15, 21539–21582, 2015

2 Experimental methods

2.1 Sampling site and period

The measurements were performed at the Finokalia station (35°32′ N, 25°67′ E; http://finokalia.chemistry.uoc.gr) of the University of Crete, which is part of the Aerosols, Clouds, and Trace gases Research Infrastructure Network (ACTRIS; http://www.actris.net/). More details about the sampling site have been provided by Mihalopoulos et al. (1997) and Sciare et al. (2003). Measurements took place from mid-August to mid-November 2012, the focus of our analysis however involves the periods of intense biomass burning influence, August to September 2012. BB plumes sampled were fresh, originating from the Greek islands and mainland (transport time 6–7 h) but also from long-range transport from the Balkans (transport time > 1 day) by using HYSPLIT backtrajectory analysis as shown in detail in Bougiatioti et al., 2014 combined with the hot spots/fire data from MODIS/Fire Information for Resource Management System (FIRMS).

2.2 Instrumentation and methodology

A Continuous Flow Stream-wise Thermal Gradient CCN Chamber (CFSTGC; Roberts and Nenes, 2005) was used in parallel with a Hygroscopic Tandem Differential Mobility Analyzer (HTDMA; Rader and McMurry, 1986) to measure the CCN number, activity and hygroscopicity of ambient aerosol for supersaturated (0.1–0.7 %) and subsaturated conditions (relative humidity, RH = 86 %), respectively. The whole system, which is illustrated in Fig. 1, sampled air with a total flow-rate of 1.8 L min^{-1}. After passing through a nafion dryer (MD-110–12S-2, Perma Pure LLC, RH < 30 %) the dried particles were selected based on their electrical mobility by a Differential Mobility Analyzer (DMA-1; TSI Model 3080; Knutson and Whitby, 1975). The sheath flow and classified aerosol outlet flow of DMA-1 were 10.8 and 1.8 L min^{-1}, respectively, while the mobility diameter was changed every 6 min between 60, 80, 100 and 120 nm.

ACPD
15, 21539–21582, 2015

The classified aerosol from DMA-1 was then split into two streams. The first stream was passed through a nafion-tube humidity exchanger where its RH was increased to 86 %. The size distribution of the RH-conditioned particles was determined by a second DMA (DMA-2; custom-made DMA using a closed-loop sheath flow with RH control; Biskos et al., 2006; Bezantakos et al., 2013) coupled with a Condensation Particle Counter (CPC, TSI Model 3772; Stolzenburg and McMurry, 1991) to measure the total number concentration of each classified particle size. The RH in both the aerosol and the sheath flow in DMA-2 was controlled by PID controllers within a ±2 % accuracy. Both DMAs in the HTDMA system were calibrated with Polystyrene Latex (PSL) spheres. The other classified stream was introduced into the CFSTGC to measure the CCN activity of particles. The CFSTGC was operated in Scanning Flow CCN Analysis (SFCA) mode (Moore and Nenes, 2009), in which the flow rate in the growth chamber changes over time, while a constant streamwise temperature difference is applied. This causes supersaturation to change continuously, allowing the rapid and continuous measurement of CCN spectra with high temporal resolution. The SFCA cycle used involved first increasing the flow rate linearly between a minimum flow rate (Q_{min} ~ 300 $cm^3\,min^{-1}$) and a maximum flow rate (Q_{max} ~ 1000 $cm^3\ min^{-1}$) over a ramp time of 60 s. The flow was maintained at Q_{max} for 10 s and then linearly decreased to Q_{min} over 60 s. Finally, the flow rate was held constant at Q_{min} for 10 s and the scan cycle was repeated. The activated droplets in the CFSTGC were counted and sized at the exit of its growth chamber with an Optical Particle Counter (OPC) that detects droplets and classifies them into 20 size bins with diameter ranging from 0.7 to 10 µm every 1 s.

The overall performance of the system was investigated with ammonium sulfate calibration aerosol following the procedure of Moore and Nenes (2009). In brief, an ammonium sulfate solution was atomized, dried, charge-neutralized and classified by DMA-1. The resulting aerosol flow was split between DMA-2 and the CFSTGC, resulting in total number at each size as well as the corresponding CCN. This provided the activation ratio, which was plotted against the instantaneous flow rate and fit to a sigmoid function. The point at which half of the particles of the selected size act as CCN corresponds to

ACPD
15, 21539–21582, 2015

a "critical flow" and the instantaneous supersaturation inside the chamber (critical supersaturation) of the classified ammonium sulfate. Repeating the procedure for several sizes of classified ammonium sulfate results in the calibration curve.

Supersaturation in the CFSTGC was calibrated in terms of the CCNC streamwise temperature difference (ΔT = 5 K), the instantaneous flow rate and the overall flow rate range. Sigmoidal activation curves of CCN vs. flow rate are obtained, and the inflection point of the sigmoid is used as the critical activation flow, Q_{50}, rate which corresponds to the critical supersaturation S_c (hence instrument supersaturation) above which particles act as CCN. The humidification in the DMA-2 was also evaluated by the growth factor measured for the calibration $(NH_4)_2SO_4$. CCN activation is characterized by the CCN to CN ratio (activation ratio), R_a, which is a function of instantaneous flow rate during a flow cycle. R_a data were fit to the sigmoidal equation:

$$R_a \equiv \frac{\mathrm{CCN}}{\mathrm{CN}} = a_0 + \frac{a_1 - a_0}{1 + (Q/Q_{50})^{-a_2}} \quad (1)$$

where a_0, a_1, a_2 and Q_{50}, are constants which describe the minimum, maximum, slope and inflection point of the sigmoidal, respectively, and Q is the instantaneous volumetric flow rate. The "critical flow rate", Q_{50}, corresponds to the instantaneous flow rate that produces a level of supersaturation required to activate the measured monodisperse aerosol, S_c. The implementation of Köhler theory presented by Moore et al. (2012a) is used to convert the critical activation flow in terms of critical supersaturation. Absolute uncertainty of the calibrated CCNC supersaturation is estimated to be ±0.04 % (Moore et al., 2012a, b). This process is repeated for many calibration aerosol sizes to obtain a comprehensive calibration.

R_a can also be expressed as a function of supersaturation using the calibration of Q vs. S as follows:

$$R_a(s) = \frac{E}{1 + (\frac{S}{S^*})^C} \quad (2)$$

ACPD
15, 21539–21582, 2015

where E is the maximum fraction of particles that activate at a given supersaturation, S is the instrument supersaturation and S^* is the characteristic critical supersaturation at which half of the classified CCN activate. In the term of Eq. (2), R_a represents a cumulative distribution of critical supersaturation for particles with dry diameter d_p (Cerully et al., 2011). Köhler theory can then be applied to transform $R_a(s)$ into accumulative distribution of hygroscopicity parameter $R_a(\kappa)$:

$$\kappa_{CCN} = \frac{4A^3}{27 d_p^3 S_c^2}, A = \frac{4 M_w \sigma_w}{RT \rho_w} \quad (3)$$

where M_w, σ_w and ρ_w are respectively the molar mass, the surface tension and the density of water, R is the universal gas constant, and T is temperature. For every critical supersaturation there is a corresponding characteristic hygroscopicity parameter, κ^*, and the probability distribution function for κ, $p^s(\kappa)$ can provide the chemical dispersion, which describes the degree of chemical heterogeneity of the CCN population (Cerully et al., 2011).

Particle hygroscopic growth at sub-saturated conditions (g_i) is obtained by:

$$g(\mathrm{RH}) = \frac{d_m(\mathrm{RH})}{d_p} \quad (4)$$

where d_m(RH) and d_p are the geometric mean mobility diameters of the sampled particles at the hydrated state (i.e. at RH = 86 %) as measured by DMA-2 and the CPC, and at the dry state selected by DMA-1 (RH < 30 %), respectively. Particle size distributions at 86 % RH were inverted using the TDMAfit algorithm (Stolzenburg and McMurry, 1988) which is also capable of distinguishing between internally and externally mixed aerosols (e.g. Bezantakos et al., 2013).

The corresponding κ_{HTDMA} values at sub-saturated conditions are calculated using:

$$\kappa_{HTDMA} = (g(\mathrm{RH})^3 - 1)\left(\frac{\exp\left(\frac{A}{g(\mathrm{RH})\cdot d_p}\right)}{\frac{RH}{100\,\%}} - 1\right) \quad (5)$$

ACPD
15, 21539–21582, 2015

with A being already defined in Eq. (3). The exponential term of this equation (i.e. the Kelvin term) is used to account for curvature effects on vapor pressure.

An average value of the hygroscopic parameter at each dry particle size, d_p, which is representative of the hygroscopic properties of the entire particle population is obtained as follows:

$$\overline{\kappa_{\mathrm{HTDMA}}} = \int_{g_{\min}}^{g_{\max}} \kappa(g_{(\mathrm{RH})}) p(g_{(\mathrm{RH})}) \mathrm{d}g_{(\mathrm{RH})} \quad (6)$$

where $\kappa(g_{(\mathrm{RH})})$ is obtained from the growth factor probability distribution using Eq. (5) and $p(g_{(\mathrm{RH})})$ is the probability of each growth factor. $g_{\min}$, $g_{\max}$ are the minimum and maximum growth factors, respectively, obtained from the growth factor probability distribution and represent the minimum and maximum g with non-zero probability value.

Chemical composition and mass concentration of non-refractory components (ammonium, sulfate, nitrate, chloride and organics) of the submicron aerosol fraction was provided by an Aerodyne Research Aerosol Chemical Speciation Monitor (ACSM; Ng et al., 2011) with a temporal resolution of 30 min. More details of the ACSM measurements can be found in Bougiatioti et al. (2014). Total absorption measurements provided the black carbon (BC) concentrations by a seven-wavelength aethalometer (Magee Scientific, AE31). From the BC measurements and using the approach of Sandradewi et al. (2008) the wood-burning and fossil fuel contribution to the total BC concentrations were calculated, using an absorption exponent of 1.1 for fossil fuel burning and 1.86 for pure wood burning. The aerosol particle size distributions from 9 to 850 nm were monitored by a custom-built scanning mobility particle sizer (SMPS; TROPOS-type, Wiedensohler et al., 2012) equipped with a condensation particle counter (CPC; TSI model 3772) that provides measurements of the aerosol size distribution every 5 min.

To support the in situ instruments, we used space-borne laser remote sensing (lidar) data from CALIOP (Mamouri et al., 2009; Winker et al., 2009) to characterize the

ACPD
15, 21539–21582, 2015

plumes emerging from the fire hot spots. The fire plume originating from the location can be tracked by HYSPLIT back-trajectory analysis (Bougiatioti et al., 2014) and lidar observations can be used to check the presence of aerosol layers and aerosol types. CALIOP is also able to provide the vertical profiles of different types of aerosols, as well as the optical properties of clouds over the globe with unprecedented spatial resolution since June 2006 (Winker et al., 2009).

3 Results and discussion

3.1 Identifying periods of biomass burning influence

Bougiatioti et al. (2014) identified the BB events analyzed here by the time evolution of absorption enhancements (BC) in the aerosol, which was further verified by FIRMS and back-trajectory analysis. During these events mass spectrometric biomass burning tracers (i.e. fragments m/z = 60 and 73) also exhibited elevated levels. Clear biomass burning contribution was identified by source apportionment using Positive Matrix Factorization (PMF) analysis for four distinct events. The BB events considered include a severe fire event that burned most of the island of Chios (19–21 August), an extensive wildfire at the Dalmatian Coast in Croatia resulting in smoke plumes that spread across the Balkans during the period 28–30 August, and, less extensive fires on the Greek islands of Euboea (3–5 September) and Andros (12–13 September).

MODIS and CALIOP measurements confirm the validity of the Bougiatioti et al. (2014) analysis, by clearly showing the origin, transport path and characteristics of the biomass burning plume from the Chios fire on 18 and 19 August 2012, respectively. Indeed, in Fig. 2a we show the MODIS true color image showing the plume emerging from the Chios fires on 18 August 1992 as obtained during its 9.39 UTC overpass over Greece (Kyzirakos et al., 2014). The blue and red lines delineate the ground track of the CALIPSO satellite during its overpass over Crete several hours later on 19 August 2012 on 00:27–00:40 and 11:34–11:47 UTC, respectively; the red

ACPD
15, 21539–21582, 2015

star shows the sampling site at Finokalia station. The CALPSO vertical profiles of the aerosol backscatter coefficient (in $km^{-1} sr^{-1}$) at 532 and 1064 nm for the two overpasses (at 00:27–00:40 and 11:34–11:47 UTC) are shown in Fig. 2b (left-hand side) together with the corresponding linear particle depolarization ratio at 532 nm obtained between 00:27:30–00:40 UTC (right-hand side). Comparing the midnight and the daytime aerosol backscatter profiles in Fig. 2b, we observe that the midnight values are 3–4 times lower than the daytime ones for altitudes up to 3 km height. In addition, the daytime observations show a discrete aerosol layer bellow 1.5 km. As for the linear particle depolarization ratio it shows a mean value of 19 % (up to 1.25 km height) and less than 6–10 % (1.25–2 km).

Finally, we made use of the classification scheme of the CALIPSO data (Omar et al., 2009) to classify the different subtypes of aerosols in the plume captured during its overpass over Crete on 19 August 2012 (00:27–00:40 UTC). This classification scheme, based on the optical and microphysical properties of the sampled aerosols indeed reveals the presence of a mixture of smoke, polluted dust and marine particles observed below a 3 km altitude (black color for smoke, brown for polluted dust and blue for marine) as shown in Fig. 2c, within the depicted area between 39° N, 24.1° E–37° N, 23.4° E, just NW of the Finokalia station and along the CALIPSO ground track. According to this classification, over Crete the presence of polluted dust (mixed with smoke and marine aerosols) prevails within the marine boundary layer, which for Finokalia is approximately 1 km (Kalivitis et al., 2007), extending up to 0.8–1.2 km height.

3.2 PM_1 composition

The average mass concentration for the whole measurement period, based on the ACSM measurements combined with BC from the aethalometer was $9.2 \pm 4.8\ \mu g\ m^{-3}$. The corresponding average concentrations for the main aerosol constituents were 2.87 ± 1.85, 0.91 ± 0.71, 2.33 ± 1.05 and $0.41 \pm 0.18\ \mu g\ m^{-3}$ for sulfate, ammonium, organics and BC respectively. Figure 3 represents the time series of the major submicron species where it can be seen that during the fire events the contribution of organics and

ACPD
15, 21539–21582, 2015

BC increased substantially (from 34.9 to 46.5 % for organics and from 6.1 to 9.5 % for BC) with a simultaneous reduction of that of sulfate. The wood burning component of BC is also provided as a reference, depicting the enhanced contribution of biomass burning during the highlighted events.

Based on Köhler theory and the calculation of the critical supersaturation, and the hygroscopicity parameter κ (Eq. 3), it is evident that the changes in the organics and sulfate mass fractions will also influence the CCN concentrations, activation fractions and hygroscopicity. These aspects are thoroughly investigated in the following sections.

3.3 CN and CCN number concentrations and biomass burning events

During four events of biomass burning-influenced air masses arriving at Finokalia, the number concentration for all particle sizes that were measured increased considerably. For most of the events and especially for the larger particle sizes, concentrations exhibited an increase that for the case of the Chios fire was around 65 %, for the Croatia fire around 50 %, the Euboea fire 88 % and the Andros fire around 150 %. This increase was also observed for the smaller particle sizes but was less pronounced. Figure 4 represents the CCN concentrations of the classified aerosol at the centroid mobility diameter measured, for the four identified fire events; (a) Chios, (b) Croatia, (c) Euboea and (d) Andros. Concentrations are given at the point of critical activation flow Q_{50} of the SFCA, corresponding to the instantaneous supersaturation, for each particle size, as described in detail in Sect. 2.2. As expected, smaller particles exhibit the higher critical supersaturation (Bougiatioti et al., 2011). It can also be seen that during the smoke influence critical supersaturations are higher, indicating that particles do not activate so readily. In order to see the direct influence of biomass burning to particle number concentrations, along with the CCN concentrations we studied the concentration of the BBOA component, identified by PMF analysis of the ACSM mass spectra. The BBOA time series depicts the arrival time of the smoke plume and the magnitude of the event, based on the measured concentration. More details about the PMF analysis can be found in Bougiatioti et al. (2014).

ACPD
15, 21539–21582, 2015

The data shown in Fig. 4 indicates that during the majority of the identified biomass burning events, CCN concentrations for the larger particles sizes increase, tracking the BBOA trend. Similar observations have been reported by Rose et al. (2010) during a biomass burning event near the mega-city Guangzhou, China during the PRIDE-PRD2006 campaign, where CCN number concentrations at lower supersaturations of S = 0.068 and 0.27 %, CCN number concentrations were higher than the study average by 90 and 8 %, respectively, which was attributed to the larger average particle sizes.

It can also be seen that that the particles that appear to be less influenced for all of the events, are those having a diameter of 60 nm. Nevertheless, for these particles it can be seen that following the influence of the Croatia fire (Fig. 4b), CCN concentration for 60 nm particles exhibit a substantial increase. This event, together with others of smaller extent, is associated with new particle formation (NFP) events. It appears that when the BB event is combined with a NPF event within a few hours, 60 nm particles are strongly influenced and their CCN concentrations increase considerably. A detailed discussion on these events and their contribution to CCN concentrations is provided by Kalivitis et al. (2015).

3.4 CCN activation fractions during fire events

As demonstrated in the preceding section, during the biomass burning events CCN number concentrations of mostly the larger particle sizes augmented, and so did the total number concentrations at the corresponding particle size, with the exception of the smaller ones. Figure 5 shows the activation fractions (CCN/CN) for three of the four particle sizes and the four considered fire events, as once more particles of 100 and 120 nm exhibit a similar behavior. In this case, instead of the BBOA factor, the concentration of the identified processed BBOA (OOA-BB) which represents the atmospherically-processed component of BBOA, is given for reference.

First of all, it can be seen that apart from the 60 nm particles, the remaining sizes appear to be unaffected by the presence of smoke, as their activation fractions at supersaturation levels as low as 0.4 % remain, more or less, stable and very close to

ACPD
15, 21539–21582, 2015

unity throughout the events. This observation implies that, almost all aerosol particles larger than 80 nm are CCN active at supersaturations higher than 0.6 %, within uncertainties. In addition, larger particles tend to be internally mixed, which can justify their high $R_a(d_p)$ at the point of their characteristic supersaturation. This can be attributed to atmospheric processing and condensation of secondary aerosol components that are usually more hygroscopic, particles are also more CCN active. The mixing state of each particle size is further investigated in the subsequent section. The same conclusion is also drawn from the data provided by Bougiatioti et al. (2011) for the same sampling site during summertime, and are verified by analysis of the chemical dispersion and HTDMA data shown in following sections.

In contrast to the above, R_a (60 nm) at 0.6 % S (and in the case of the Chios fire R_a (80 nm) at 0.4 % S) exhibits the highest variability, with ratios reaching at some cases even 40 %. This indicates that a substantial fraction of the smaller particle sizes may well be an external mixture with low hygroscopicity particles that do not act as CCN up to ~ 0.6 % supersaturation. Indeed, the lower activation fractions occur for the strongest events where the time for transport and aging is limited. This aspect is further supported by the particle chemical dispersion retrievals discussed in the following section.

The mixing state of the different sampled particle sizes is also investigated by the HTDMA measurements (Sect. 3.6). For reference, the concentration of the OOA-BB factor is also provided in Fig. 5, which represents an oxygenated organic aerosol which is derived from the atmospheric processing of biomass burning organic aerosol (Bougiatioti et al., 2014). It can be seen that as concentrations of the OOA-BB start to increase, the R_a (60 nm) at ~ 0.6 % S starts to diminish. This is also the case for the Croatia fire, even though the CCN concentrations did not fluctuate much from background levels because of the longer transport. It appears, thus that larger particles are mostly internally mixed, as also seen by their high activation ratios, while small particles could be externally mixed populations. This behavior is further discussed in the following section.

ACPD
15, 21539–21582, 2015

3.5 Hygroscopicity and chemical heterogeneity during the biomass burning events

The characteristic hygroscopicity parameters, κ^*, derived from the CCN measurements for all particle sizes and for the four selected fire events are presented in Fig. 6. As a reference for the arrival time and magnitude of the smoke, the concentration of the BBOA factor is also shown in the figure. The smaller particles have the lowest κ_{CCN} values, and hygroscopicity consistently increased with size. This hygroscopicity trend has also been observed elsewhere (Dusek et al., 2010; Cerully et al., 2011; Levin et al., 2012; Paramonov et al., 2013; Liu et al., 2014), and is attributed to the enrichment in organic material of sub-100 nm particles. Most of the accumulation mode particles result from condensation of secondary sulfates, nitrates and organics from the gas phase and coagulation of smaller particles (Seinfeld and Pandis, 2006). Accumulation mode particles can also result from cloud processing but as at the given time of the study, cloud coverage in the boundary layer and aloft is limited, we assume that this mechanism is not as important. This is further supported by the lack of a modal separation around 60 nm, which indicates that cloud processing is not contributing to the chemical dispersion tendency seen here. On the other hand, particles larger than 100 nm are more aged than the smaller particles and more immediately associated with BB plumes and the atmospheric processing they undergo (Kalivitis et al., 2015). The hygroscopicity parameter for 100 and 120 nm particles are very similar, while 80 nm particles are in between the lowest and highest κ_{CCN} values, an indication of size-dependent chemical composition of components with different hygroscopicities.

Figure 6 also shows that during the arrival of the biomass burning-laden air masses, κ values of all particle size ranges within 0.2–0.3. This observation is consistent with values observed from chamber experiments of fresh and aged biomass burning aerosol and in-situ studies from the field. Engelhart et al. (2012) performed a study where 12 different biomass fuels commonly burnt in North American wildfires were used to characterize their respective hygroscopicity. They found that while κ of freshly emitted

ACPD
15, 21539–21582, 2015

BBOA prior to photochemical aging covered a range from 0.06 to 0.6, after a few hours of photochemical processing, the variability of biomass burning κ values from the different fuels was reduced and hygroscopicity converged to a value of 0.2 ± 0.1 (Cerully et al., 2011; Engelhart et al., 2012).

During the fire events the contribution of organics and BC to the submicron aerosol mass fraction increased significantly while the presence of sulfate declined. This is expected to influence the CCN activity of the sampled aerosol particles as it would cause variations in the inorganic and organic mass fractions. It has already been established that as the organic mass fraction of aerosol increases, the κ value of primary aerosol decreases (Petters et al., 2009; Engelhart et al., 2012). With photochemical aging, the increased oxygenation of the freshly emitted BBOA may influence the hygroscopicity of the organic components, but the concurrent increase of the inorganic fraction of the aerosol contributes to the observed increase of κ_{CCN} (inorganic content vs. aging).

In order to examine the role of atmospheric processing and aging to the sampled aerosol, we studied the chemical dispersion $\sigma(\kappa)$, and its dependence on particle size. As normal operation uncertainties and the DMA transfer function can induce a broadening of $R_a(s)$ and $R_a(\kappa)$ and contribute to $\sigma(\kappa)$, the inferred $\sigma(\kappa)$ contains a fairly constant instrument offset and a time-dependent constituent that is representative of the real chemical variability. This offset value (instrument limit) has been calculated to be roughly 0.25 by Cerully et al. (2011). Table 1 shows the calculated chemical dispersion, in terms of $\sigma(\kappa)/\kappa$, for the four fire events and the measured particle sizes. It is immediately apparent that the chemical dispersion is reduced with increasing particle size. 60 nm particles exhibit the highest dispersion and especially the ones from the Chios fire, suggesting that the smaller particles retain their characteristics for a longer period and their aging takes longer that for the larger particles. The 80 and 100 nm particles from the Chios fire have high $\sigma(\kappa)/\kappa$ values while the ones from Euboea and Andros have considerably lower values, demonstrating the magnitude of the Chios fire and the degree of atmospheric processing that has taken place. Finally, 120 nm particles always have a low chemical dispersion, with $\sigma(\kappa)/\kappa$ values close to the instrument limit.

ACPD
15, 21539–21582, 2015

This behavior of the small particles may be partially due to the coagulation of ultrafine particles which are present in biomass burning plumes, as the coagulation mostly occurs for smaller particles and increases the external mixing of those particles by bringing together particles of different nature. It is also possible that organic compounds that are emitted during biomass burning events and undergo atmospheric processing during their transport, could condense on the existing particles, contributing thus to their mass. This condensational growth tends to render particles more chemically uniform, and if this condensation takes place in the smaller particle range it would have a larger impact on their chemical composition, than for the larger ones. Both condensational growth and coagulation processes can take place, with the overall observed behavior depending on which process is predominant (Healy et al., 2014). Based on the surface area distributions (Fig. S1 in the Supplement) it occurred that the peak of the surface area is around 200 nm. With the surface area distribution being constant, one can argue that larger particle sizes would receive most of the condensational mass. For the Chios fire, where the peak in the number size distribution is in the smaller particle range, coagulation is more effective for the 60 and 80 nm particles. This is further supported by the elevated chemical dispersion of those sizes caused by the coagulation and the lower chemical dispersion of 100 and 120 nm particles caused by the condensation. On the other hand, during the Euboea fire where the peak in the number size distribution is closer to the peak of the surface area distribution, it seems that mostly the 60 nm particles are subject to coagulation. Larger particles could be affected by both condensation and coagulation but the chemical dispersion as a function of particle size indicates that mostly condensation processes dominate in the BB plumes. For this reason, the hygroscopicity parameters are calculated for all events and particle sizes in the following section.

3.6 Particle growth factors during the fire events

From the concurrent HTDMA growth factor measurements at sub-saturated conditions we calculated the corresponding κ_{HTDMA} values. During the focus period, the grand ma-

ACPD
15, 21539–21582, 2015

jority of the HTDMA data exhibited unimodal distributions, indicating that all selected particle fractions were internally mixed. Bimodal distributions were scarce and therefore are not taken into account for this specific study. Average CFSTGC-derived κ_{CCN} values and HTDMA-derived κ_{HTDMA} values for the selected particles sizes are given in Table 2. On average, κ_{HTDMA} values are somewhat lower than the respective κ_{CCN} values for the smaller particles, while the difference between them is larger for the larger particle sizes. Nevertheless, both time series follow the same trend and values are consistent within ±30 % ($\kappa_{HTDMA} = 0.854 \cdot \kappa_{CCN}$, $R^2 = 0.87$; Fig. S2 in the Supplement). Given that the solution of the resulting droplets may be non-ideal, the constituents may be partially soluble and the phases may not be completely separated, it is not surprising that the HTDMA-derived κ_{HTDMA} values are somewhat lower. Therefore, these differences are well within the range of possible uncertainties and are common when comparing CFSTGC and HTDMA-derived κ values (e.g. Prenni et al., 2007; Massoli et al., 2010; Cerully et al., 2011).

Apart from the hygroscopicity parameter, κ_{HTDMA}, from the concurrent HTDMA measurements the mixing state of the sampled particle sizes were also determined. During the two most intense fire events where the smoke plume had the least transit and atmospheric processing time (i.e. during the Chios and Euboea fire) all sizes exhibited two different hygroscopic modes (Tables 3 and 4; Fig. S3 in the Supplement). These distinct modes were not observed during the rest of the events, probably due to the lower intensity of the other events and the longer transport time. Figure 7 portrays in the left-hand panels the $\overline{\kappa_{HTDMA}}$ (estimated using Eq. 6) for the sampled particle sizes during the Chios and Euboea fires. The right-hand panels show the respective particle size distributions obtained by the concurrent SMPS measurements, revealing the presence of different particle modes. During the arrival of the smoke-influenced air masses, there is a decrease in the hygroscopicity of all measured sizes. At the same time a bimodal distribution was observed by the SMPS (far right panels), indicative of two groups of particles, probably freshly emitted particles (i.e. smaller mode) in combination with larger, more processed ones. Adler et al. (2011) had also observed a shift

ACPD
15, 21539–21582, 2015

in the average mode diameter of size distributions from 86 ± 8 nm for freshly-emitted BBOA to 114 ± 7 nm for processed BBOA. This further supports the observed higher chemical dispersion found in the smaller particle sizes, presented in the previous section.

A similar behavior when the sampled particles influenced by biomass burning were exposed to sub-saturated conditions has been reported by Rissler et al. (2006). In those measurements the hygroscopic growth of the sampled particles when exposed at 90 % RH showed that there was an external mixture of a nearly hydrophobic ($g_{(RH)}$ = 1.09 for 100 nm particles) and a moderately hygroscopic ($g_{(RH)}$ = 1.26) population. This reinforces our observations from the CCN measurements, where in supersaturated conditions, the activation fraction of mainly the 60 nm particles decreased significantly under influence of the smoke. A possible explanation why the activation fractions of the other size ranges seem to be unaffected by the smoke may be the number fraction of the two modes in each size, combined with the occurrence of these two modes. If the presence of the bimodal samples is limited (less than 30 %), then even though the fraction of the less hygroscopic mode may be as high as 45 %, the overall activation fractions might not be influenced. For the first event (20–21/8) which was the most intense, the externally mixed samples represent almost 25 % of the total sampled aerosol, with the occurrence of the bimodal samples increasing with increasing diameter (Table 3). It appears that in the bimodal samples the less hygroscopic mode initially dominates followed by a progressive dominance of the hygroscopic mode. It also appears that the increase in the less hygroscopic fraction coincides with the plume arrival time and the increase of the BBOA component, further supporting our findings of external mixing. During the second event (03–05/9) the bimodal samples increase, once more, with increasing diameter (5 % for 60 nm to 28 % for 120 nm particles) with the less hygroscopic fraction being dominant in approximately 33 % of the samples, although this more hygroscopic mode has a κ_{HTDMA} value of 0.2 during the plume arrival time (Table 4). The more hygroscopic mode is therefore dominant in number for all sampled particles, which would explain that the activation fraction of the larger ac-

ACPD
15, 21539–21582, 2015

cumulation mode particles are not significantly affected by the presence of the less hygroscopic mode. On the other hand, the reason for the reduction of the activation fraction of 60 nm particles, apart from their hygroscopicity, can also be their size, as during the events, the less hygroscopic mode is probably not activated, thus not detected by the CCN. This is not the case for the larger particles, as for example, 80 nm particles having $\kappa_{\mathrm{HTDMA}} = 0.06$ will activate at a critical supersaturation of 0.67 %.

3.7 Inferring size-dependent chemical composition and organic hygroscopicity

Assuming that the total aerosol hygroscopicity can be represented as the sum of the contribution of the different aerosol components:

$$\kappa = \sum_j \varepsilon_j \kappa_j \tag{7}$$

where ε_j and κ_j are the volume fraction and hygroscopicity of each species, respectively (Petters and Kreidenweis, 2007). With the use of this equation, and by assuming that the aerosol is a mixture of an organic and inorganic component, with the inorganic component being represented by ammonium sulfate, the total measured hygroscopicity, can be expressed by the sum:

$$\kappa = \varepsilon_{\mathrm{inorg}} \kappa_{\mathrm{inorg}} + \varepsilon_{\mathrm{org}} \kappa_{\mathrm{org}} \tag{8}$$

Prior studies at Finokalia have determined $\kappa_{\mathrm{org}} = 0.158$ and $\kappa_{\mathrm{inorg}} = 0.6$. Assuming this still applies and $\varepsilon_{\mathrm{inorg}} + \varepsilon_{\mathrm{org}} = 1$, Eq. (8) can be used to infer the volume fractions of organics and ammonium sulfate for the 4 different sizes, excluding the days of direct biomass burning influence. From this we obtain that 60 nm particles, on average, are composed of 82 % organics and 18 % ammonium sulfate; 80 nm particles of 44 % organics and 55 % ammonium sulfate, and, the larger particles are mainly composed of ammonium sulfate (67 and 78 % for 100 and 120 nm particles, respectively). This reinforces our conclusion based on the hygroscopicity measurements that the smaller

ACPD
15, 21539–21582, 2015

particles are mostly composed of organic material. These observations are in agreement with similar observations reported by Bezantakos et al. (2013) in the region of the Northern Aegean Sea.

The above approach can also be applied to the data from the fire events, as follows: we use only the larger size (120 nm) as from the former CCN studies in the area it was established that the hygroscopicity of the larger particles is close to the "bulk" hygroscopicity of the sampled aerosol (PM_1), which is constrained from the ACSM measurements (Bougiatioti et al., 2011). To evaluate the importance of the assumptions made in inferring the organic hygroscopicity from chemical composition, κ_{org} was additionally determined by applying Eq. (8), for the 120 nm particles, where a set of κ equations is produced ($n = 228$). Multivariable regression analysis is subsequently applied in order to determine the organic and inorganic component of the total hygroscopicity during the fire events. Based on the results, $\kappa_{inorg} = 0.61 \pm 0.03$ and $\kappa_{org} = 0.137 \pm 0.02$, values which are very similar to values determined by Bougiatioti et al. (2009, 2011).

Taking the analysis one step further, we attempt a source apportionment of the organic hygroscopicity, by its attribution to different factors. Positive Matrix Factorization (PMF) analysis was applied to the time series of data from the direct influence from biomass burning. A detailed discussion of the PMF results can be found in Bougiatioti et al. (2014). During the focus period, 3 subtypes of organic aerosol (OA) were identified, namely biomass burning OA (BBOA), an OOA associated with biomass burning (OOA-BB) and a highly oxygenated OOA, having a relative contribution of 22, 32 and 46 %, respectively. With the chemical composition measurements of the ACSM for the larger particle size (120 nm) combined with the respective κ_{CCN} we use the following equation to determine the hygroscopicity parameter of each factor:

$$\kappa = (1 - \varepsilon_{org})\kappa_{inorg} + \varepsilon_{BBOA}\kappa_{BBOA} + \varepsilon_{OOA\text{-}BB}\kappa_{OOA\text{-}BB} + \varepsilon_{OOA}\kappa_{OOA} \quad (9)$$

Once again a set of 228 κ equations is produced and multivariable regression analysis is applied in order to deconvolve the organic hygroscopicity to its 3 subtypes. It occurs that $\kappa_{inorg} = 0.62 \pm 0.04$, $\kappa_{BBOA} = 0.057 \pm 0.07$, $\kappa_{OOA\text{-}BB} = 0.138 \pm 0.11$ and

ACPD
15, 21539–21582, 2015

$\kappa_{OOA} = 0.169 \pm 0.09$. It is interesting to see that the inferred hygroscopicity for the freshly-emitted BBOA is very close to the hygroscopicity obtained by the HTDMA for the less hygroscopic component when two particle populations were present during the events (Tables 3 and 4, Sect. 3.6). When comparing the obtained hygroscopicity with the level of oxidation of each factor (O : C = 0.2 for BBOA, 0.9 for OOA-BB and 1.2 for OOA; Bougiatioti et al., 2014) it occurs that the less hygroscopic component is also the least oxygenated and hygroscopicity increases with increasing O : C ratio. The calculated values are also comparable to the κ obtained by Chang et al. (2010) for the oxygenated organic component (OOA-1, OOA-2 and BBOA) of rural aerosol ($\kappa_{ox} = 0.22 \pm 0.04$). They also found increased hygroscopicity with increasing ageing and degree of oxidation. Furthermore, the total organic hygroscopicity is very similar to the hygroscopicity of the processed organic aerosol components, which make up almost 80 % of the organic aerosol. Finally, it seems the biomass burning organic aerosol becomes more hygroscopic, by almost a factor of two, with atmospheric processing.

Using the average diurnal profiles obtained from the PMF analysis combined with the corresponding mass fractions of each component and the inferred hygroscopicity parameter of each, we estimated the contribution of each factor to the overall κ_{org} and the total aerosol hygroscopicity. Figure 8 presents the resulting diurnal profiles and it is clear that the grand majority of the organic hygroscopicity originates from the aged, very oxidized OOA. BBOA contributes around 7 % to the organic hygroscopicity (2.2 % to the overall aerosol hygroscopicity), which is small but not negligible, as it can be seen that when the BBOA contribution is the highest, there is an important decrease in the κ_{org}. Overall, organic aerosol associated with biomass burning can account for almost 35 % of the organic hygroscopicity. By using the approach of Guo et al. (2015) where particle water is predicted using meteorological observations (relative humidity, temperature), aerosol composition and thermodynamic modeling (ISORROPIA-II; Fountoukis and Nenes, 2007), the LWC associated with the organic fraction is calculated. It occurs that even though the freshly-emitted BBOA contributes merely 1.2 % to the total organic water of the aerosol, the corresponding contribution of the processed

ACPD
15, 21539–21582, 2015

OOA-BB is almost 33 %. It is therefore clear that in the presence of biomass burning aerosol, both aerosol hygroscopicity but LWC as well may be influenced, thus affecting the overall direct and indirect aerosol radiative effects.

4 Summary and conclusions

This study provides CCN concentrations, hygroscopicity and mixing state of size-selected aerosol particles influenced by biomass burning during summertime over the eastern Mediterranean. For the case of the most intense event the presence of smoke was clearly identified by CALIPSO laser remote sensing observations for the most intense event. Overall, during the selected events, the contribution of organics and BC increased significantly while the concentration of sulfates decreased. This is shown also to affect the hygroscopicity of the particles. The fire events had a direct influence to the total CN and CCN concentrations, where especially the larger particle sizes (larger than 100 nm) exhibited an increase in absolute number of more than 50 %. At the same time, the activation fractions of the smaller particles (60–80 nm) at 0.6 % S appeared to be affected by the smoke, with ratios being well below unity. Based on the observations it is inferred that organic compounds that are less CCN-active, are the dominant component of 60 nm particles (82 % of mass) while particles larger than 100 nm are mainly composed of ammonium sulfate. This was verified by the hygroscopicity analysis, where 60 nm particles exhibited the lowest hygroscopicity.

Nevertheless, during the arrival of the biomass-burning-laden air masses, the hygroscopicity parameters of all particle sizes converged to values in the range of 0.2–0.3, which can be attributed to different chemical composition of all particles during these events. Based on chemical dispersion analysis it occurred that smaller particles exhibit higher chemical dispersion and retain their characteristics for longer, compared to larger ones that appear more homogeneous. This can be due to the fact that coagulation likely promotes the chemical dispersion at smaller sizes, while the condensation of organics tends to make larger particles more uniform. Despite that, samples with

ACPD
15, 21539–21582, 2015

two distinct populations, one having lower and one somewhat higher hygroscopicity, do appear during the fire events. Nevertheless, their occurrence is limited and the overall activation of particles appears to be unaffected by the presence of these two populations. Overall we can conclude that 60 nm particles were mostly composed by less hygroscopic species, even when they have undergone atmospheric processing and they were internally mixed, making it more difficult for them to activate because of their size and hygroscopicity even at the highest level of supersaturation. It appears that the dominant process in this particle range is coagulation, rendering small particles less uniform, with increased chemical dispersion.

On the other hand, larger particles were composed of more hygroscopic species, which either condensational growth or atmospheric aging yielded an internal mixture with lower chemical dispersion. This supports the assumption of external mixing for smaller particles originating from biomass burning with decreased activation fractions and provides a plausible explanation of why larger particles appear not to be affected as far as their CCN-activity is concerned.

Finally, using multivariable regression analysis and the volume fractions of organics and ammonium sulfate for the different particle sizes, we inferred the hygroscopicity of the organic fraction and found it equal to 0.115 ± 0.017, which is comparable to the value of 0.2 ± 0.1 determined for processed biomass burning aerosol. Using the results obtained from the source apportionment of the organic fraction we were able to deconvolve the organic hygroscopicity to its 3 subtypes. The hygroscopicity of freshly-emitted BBOA was found to be around 0.06, while the hygroscopicity of atmospherically-processed BBOA and highly oxidized organic aerosol was found to be 0.14 and 0.17, respectively. The inferred hygroscopicity of each component are in line with the corresponding level of oxidation of each component, and the overall organic hygroscopicity is close to the hygroscopicity derived for the processed organic aerosol. Thus, the organic fraction of biomass burning aerosol becomes more hygroscopic with atmospheric aging. Overall, organic aerosol associated with biomass burning (freshly emitted and processed) can account for almost 10 % of the total aerosol hygroscopic-

ACPD
15, 21539–21582, 2015

ity (2.2 and 7.6 %, respectively). Taking into account the fact that organic aerosol may have important contribution to the fine-particle water (Guo et al., 2015), it is estimated that the liquid water content contribution of BBOA and OOA-BB is of the order of 1.2 and 32.6 % of the total organic water of the aerosol. This has important implications to aerosol chemistry, as aerosol water can provide the medium for heterogeneous reactions, but also can contribute to the aerosol direct and indirect radiative effect.

The Supplement related to this article is available online at doi:10.5194/acpd-15-21539-2015-supplement.

Acknowledgements. The work of A. Bougiatioti, A. Papayannis, P. Kokkalis was supported by the "MACAVE" research project which is implemented within the framework of the action Supporting of Postdoctoral Researchers of the Operational Program Education and Lifelong Learning (action's beneficiary: general Secretariat for Research and Technology), and is co-financed by the European Social Fund (ESF) and the Greek State. This research has also been co-financed by the European Union (European Social Fund – ESF) and Greek national funds through the Operational Program "Education and Lifelong Learning" of the National Strategic Reference Framework (NSRF) – Research Funding Program: THALES, Investing in knowledge society through the European Social Fund. The financial support by the European Community through the ACTRIS Research Infrastructure Action and Bacchus project under the 7th Framework Programme (Grant Agreements no 262254 and 603445, respectively) are gratefully acknowledged. A. Nenes acknowledges support from a Georgia Power Faculty Scholar Chair and a Cullen-Peck Faculty Fellowship.

References

Adler, G., Flores, J. M., Abo Riziq, A., Borrmann, S., and Rudich, Y.: Chemical, physical, and optical evolution of biomass burning aerosols: a case study, Atmos. Chem. Phys., 11, 1491–1503, doi:10.5194/acp-11-1491-2011, 2011.

ACPD
15, 21539–21582, 2015

Andreae, M. O., Rosenfeld, D., Artaxo, P., Costa, A. A., Frank, G. P., Longo, K. M., and Silva Dias, M. A. F.: Smoking rain clouds over the Amazon, Science, 303, 1337–1342, 2004.

Asa-Awuku, A., Moore, R. H., Nenes, A., Bahreini, R., Holloway, J. S., Brock, C. A., Middlebrook, A. M., Ryerson, T., Jimenez, J., DeCarlo, P., Hecobian, A., Weber, R. Stickel, R., Tanner, D. J., and Huey, L. G.: Airborne cloud condensation nuclei measurements during the 2006 Texas air quality study, J. Geophys. Res., 116, D11201, doi:10.1029/2010JD014874, 2010.

Bezantakos, S., Barmpounis, K., Giamarelou, M., Bossioli, E., Tombrou, M., Mihalopoulos, N., Eleftheriadis, K., Kalogiros, J., D. Allan, J., Bacak, A., Percival, C. J., Coe, H., and Biskos, G.: Chemical composition and hygroscopic properties of aerosol particles over the Aegean Sea, Atmos. Chem. Phys., 13, 11595–11608, doi:10.5194/acp-13-11595-2013, 2013.

Biskos, G., Paulsen, D., Russell, L. M., Buseck, P. R., and Martin, S. T.: Prompt deliquescence and efflorescence of aerosol nanoparticles, Atmos. Chem. Phys., 6, 4633–4642, doi:10.5194/acp-6-4633-2006, 2006.

Bougiatioti, A., Fountoukis, C., Kalivitis, N., Pandis, S. N., Nenes, A., and Mihalopoulos, N.: Cloud condensation nuclei measurements in the marine boundary layer of the Eastern Mediterranean: CCN closure and droplet growth kinetics, Atmos. Chem. Phys., 9, 7053–7066, doi:10.5194/acp-9-7053-2009, 2009.

Bougiatioti, A., Nenes, A., Fountoukis, C., Kalivitis, N., Pandis, S. N., and Mihalopoulos, N.: Size-resolved CCN distributions and activation kinetics of aged continental and marine aerosol, Atmos. Chem. Phys., 11, 8791–8808, doi:10.5194/acp-11-8791-2011, 2011.

Bougiatioti, A., Stavroulas, I., Kostenidou, E., Zarmpas, P., Theodosi, C., Kouvarakis, G., Canonaco, F., Prévôt, A. S. H., Nenes, A., Pandis, S. N., and Mihalopoulos, N.: Processing of biomass-burning aerosol in the eastern Mediterranean during summertime, Atmos. Chem. Phys., 14, 4793–4807, doi:10.5194/acp-14-4793-2014, 2014.

Carlton, A. G. and Turpin, B. J.: Particle partitioning potential of organic compounds is highest in the Eastern US and driven by anthropogenic water, Atmos. Chem. Phys., 13, 10203–10214, doi:10.5194/acp-13-10203-2013, 2013.

Cerully, K. M., Raatikainen, T., Lance, S., Tkacik, D., Tiitta, P., Petäjä, T., Ehn, M., Kulmala, M., Worsnop, D. R., Laaksonen, A., Smith, J. N., and Nenes, A.: Aerosol hygroscopicity and CCN activation kinetics in a boreal forest environment during the 2007 EUCAARI campaign, Atmos. Chem. Phys., 11, 12369–12386, doi:10.5194/acp-11-12369-2011, 2011.

ACPD
15, 21539–21582, 2015

Cerully, K. M., Bougiatioti, A., Hite Jr., J. R., Guo, H., Xu, L., Ng, N. L., Weber, R., and Nenes, A.: On the link between hygroscopicity, volatility, and oxidation state of ambient and water-soluble aerosol in the Southeastern United States, Atmos. Chem. Phys. Discuss., 14, 30835–30877, doi:10.5194/acpd-14-30835-2014, 2014.

Chang, R. Y.-W., Slowik, J. G., Shantz, N. C., Vlasenko, A., Liggio, J., Sjostedt, S. J., Leaitch, W. R., and Abbatt, J. P. D.: The hygroscopicity parameter (κ) of ambient organic aerosol at a field site subject to biogenic and anthropogenic influences: relationship to degree of aerosol oxidation, Atmos. Chem. Phys., 10, 5047–5064, doi:10.5194/acp-10-5047-2010, 2010.

Dusek, U., Frank, G. P., Curtius, J., Drewnick, F., Schneider, J., Kürten, A., Rose, D., Andreae, M. O., Borrmann, S., and Pöschl, U.: Enhanced organic mass fraction and decreased hygroscopicity of cloud condensation nuclei (CCN) during NPF events, Geophys. Res. Lett., 37, L03804, doi:10.1029/2009GL040930, 2010.

Engelhart, G. J., Hennigan, C. J., Miracolo, M. A., Robinson, A. L., and Pandis, S. N.: Cloud condensation nuclei activity of fresh primary and aged biomass burning aerosol, Atmos. Chem. Phys., 12, 7285–7293, doi:10.5194/acp-12-7285-2012, 2012.

Fountoukis, C. and Nenes, A.: ISORROPIA II: a computationally efficient thermodynamic equilibrium model for K^+–Ca^{2+}–Mg^{2+}–NH_4^+–Na^+–SO_4^{2-}–NO_3^-–Cl^-–H_2O aerosols, Atmos. Chem. Phys., 7, 4639–4659, doi:10.5194/acp-7-4639-2007, 2007.

Guo, H., Xu, L., Bougiatioti, A., Cerully, K. M., Capps, S. L., Hite Jr., J. R., Carlton, A. G., Lee, S.-H., Bergin, M. H., Ng, N. L., Nenes, A., and Weber, R. J.: Fine-particle water and pH in the southeastern United States, Atmos. Chem. Phys., 15, 5211–5228, doi:10.5194/acp-15-5211-2015, 2015.

Healy, R. M., Riemer, N., Wenger, J. C., Murphy, M., West, M., Poulain, L., Wiedensohler, A., O'Connor, I. P., McGillicuddy, E., Sodeau, J. R., and Evans, G. J.: Single particle diversity and mixing state measurements, Atmos. Chem. Phys., 14, 6289–6299, doi:10.5194/acp-14-6289-2014, 2014.

Hildebrandt, L., Engelhart, G. J., Mohr, C., Kostenidou, E., Lanz, V. A., Bougiatioti, A., DeCarlo, P. F., Prevot, A. S. H., Baltensperger, U., Mihalopoulos, N., Donahue, N. M., and Pandis, S. N.: Aged organic aerosol in the Eastern Mediterranean: the Finokalia Aerosol Measurement Experiment – 2008, Atmos. Chem. Phys., 10, 4167–4186, doi:10.5194/acp-10-4167-2010, 2010.

ACPD
15, 21539–21582, 2015

Kalivitis, N., Gerasopoulos, E., Vrekoussis, M., Kouvarakis, G., Kubilay, N., Hatzianastassiou, N., Vardavas, I., and Mihalopoulos, N.: Dust transport over the eastern Mediterranean derived from total ozone mapping spectrometer, aerosol robotic network, and surface measurements, J. Geophys. Res.-Atmos., 112, D03202, doi:10.1029/2006JD007510, 2007.

Kalivitis, N., Kerminen, V.-M., Kouvarakis, G., Stavroulas, I., Bougiatioti, A., Nenes, A., Manninen, H. E., Petäjä, T., Kulmala, M., and Mihalopoulos, N.: Atmospheric new particle formation as source of CCN in the Eastern Mediterranean marine boundary layer, Atmos. Chem. Phys. Discuss., 15, 11143–11178, doi:10.5194/acpd-15-11143-2015, 2015.

Knutson, E. O. and Whitby, K. T.: Aerosol classification by electric mobility: Apparatus, theory, and applications, J. Aerosol Sci., 6, 443–451, 1975.

Kyzirakos, K., Karpathiotakis, M., Garbis, G., Nikolaou, C., Bereta, K., Papoutsis, I., Herekakis, T., Michail, D., Koubarakis, M., and Kontoes, C.: Wild fire monitoring using satellite images, ontologies and linked geospatial data, Web Semantics: Science, Services and Agents on the World Wide Web, 24, 18–26, 2014.

Levin, E. J. T., Prenni, A. J., Petters, M. D., Kreidenweis, S. M., Sullivan, R. C., Atwood, S. A., Ortega, J., DeMott, P. J., and Smith, J. N.: An annual cycle of size-resolved aerosol hygroscopicity at a forested site in Colorado, J. Geophys. Res., 117, D06201, doi:10.1029/2011JD016854, 2012.

Liu, H. J., Zhao, C. S., Nekat, B., Ma, N., Wiedensohler, A., van Pinxteren, D., Spindler, G., Müller, K., and Herrmann, H.: Aerosol hygroscopicity derived from size-segregated chemical composition and its parameterization in the North China Plain, Atmos. Chem. Phys., 14, 2525–2539, doi:10.5194/acp-14-2525-2014, 2014.

Mamouri, R. E., Amiridis, V., Papayannis, A., Giannakaki, E., Tsaknakis, G., and Balis, D. S.: Validation of CALIPSO space-borne-derived attenuated backscatter coefficient profiles using a ground-based lidar in Athens, Greece, Atmos. Meas. Tech., 2, 513–522, doi:10.5194/amt-2-513-2009, 2009.

Mamouri, R. E., Papayannis, A., Amiridis, V., Müller, D., Kokkalis, P., Rapsomanikis, S., Karageorgos, E. T., Tsaknakis, G., Nenes, A., Kazadzis, S., and Remoundaki, E.: Multi-wavelength Raman lidar, sun photometric and aircraft measurements in combination with inversion models for the estimation of the aerosol optical and physico-chemical properties over Athens, Greece, Atmos. Meas. Tech., 5, 1793–1808, doi:10.5194/amt-5-1793-2012, 2012.

Massoli, P., Lambe, A. T., Ahern, A. T., Williams, L. R., Ehn, M., Mikkilä, J., Canagaratna, M. R., Brune, W. H., Onasch, T. B., Jayne, J. T., Petäjä, T., Kulmala, M., Laaksonen, A., Kolb, C. E.,

ACPD
15, 21539–21582, 2015

Davidovits, 5 P., and Worsnop, D. R.: Relationship between aerosol oxidation level and hygroscopic properties of laboratory generated secondary organic aerosol (SOA) particles, Geophys. Res. Lett., 37, L24801, doi:10.1029/2010GL045258, 2010.

Mihalopoulos, N., Stephanou, E., Kanakidou, M., Pilitsidis, S., and Bousquet, P.: Tropospheric aerosol ionic composition above the Eastern Mediterranean area, Tellus B, 49, 314–326, 1997.

Moore, R. H. and Nenes, A.: Scanning flow CCN analysis – a method for fast measurements of CCN spectra, Aerosol Sci. Tech., 43, 1192–1207, 2009.

Moore, R. H., Cerully, K., Bahreini, R., Brock, C. A., Middelbrook, A. M., and Nenes, A.: Hygroscopicity and composition of California CCN during summer 2010, J. Geophys. Res., 117, D00V12, doi:10.1029/2011JD017352, 2012a.

Moore, R. H., Raatikainen, T., Langridge, J. M., Bahreini, R., Brock, C. A., Holloway, J. S., Lack, D. A., Middlebrook, A. M., Perring, A. E., Schwarz, J. P., Spackman, J. R., and Nenes, A.: CCN spectra, hygroscopicity, and droplet activation kinetics of secondary organic aerosol resulting from the 2010 deepwater horizon oil spill, Environ. Sci. Technol., 46, 3093–3100, 2012b.

Ng, N. L., Herndon, S. C., Trimborn, A., Canagaratna, M. R., Croteau, P. L., Onasch, T. B., Sueper, D., Worsnop, D. R., Zhang, Q., Sun, Y. L., and Jayne, J. T.: An aerosol chemical speciation monitor (ACSM) for routine monitoring of the composition and mass concentration of ambient aerosol., Aerosol Sci. Tech., 45, 780–794, 2011.

Nguyen, T. B., Coggon, M. M., Flagan, R. C., and Seinfeld, J. H.: Reactive uptake and photo-Fenton oxidation of glycolaldehyde in aerosol liquid water, Environ. Sci. Technol., 47, 4307–4316, doi:10.1021/es400538j, 2013.

Omar, A. H., Winker, D. M., Kittaka, C., Vaughan, M. A., Liu, Z. Y., Hu, Y. X., Trepte, C. R., Rogers, R. R., Ferrare, R. A., Lee, K. P., Kuehn, R. E., and Hostetler, C. A.: The CALIPSO automated aerosol classification and lidar ratio selection algorithm, J. Atmos. Ocean. Tech., 26, 1994–2014, doi:10.1175/2009jtecha1231.1, 2009.

Paramonov, M., Aalto, P. P., Asmi, A., Prisle, N., Kerminen, V.-M., Kulmala, M., and Petäjä, T.: The analysis of size-segregated cloud condensation nuclei counter (CCNC) data and its implications for cloud droplet activation, Atmos. Chem. Phys., 13, 10285–10301, doi:10.5194/acp-13-10285-2013, 2013.

ACPD
15, 21539–21582, 2015

Petters, M. D. and Kreidenweis, S. M.: A single parameter representation of hygroscopic growth and cloud condensation nucleus activity, Atmos. Chem. Phys., 7, 1961–1971, doi:10.5194/acp-7-1961-2007, 2007.

Petters, M. D., Wex, H., Carrico, C. M., Hallbauer, E., Massling, A., McMeeking, G. R., Poulain, L., Wu, Z., Kreidenweis, S. M., and Stratmann, F.: Towards closing the gap between hygroscopic growth and activation for secondary organic aerosol – Part 2: Theoretical approaches, Atmos. Chem. Phys., 9, 3999–4009, doi:10.5194/acp-9-3999-2009, 2009.

Prenni, A. J., Petters, M. D., Kreidenweis, S. M., DeMott, P. J., and Ziemann, P. J.: Cloud droplet activation of secondary organic aerosol, J. Geophys. Res., 112, D10223, doi:10.1029/2006JD007963, 2007.

Rader, D. J. and McMurry, P. H.: Application of the tandem differential mobility analyzer to studies of droplet growth or evaporation, J. Aerosol Sci., 17, 771–787, 1986.

Remy, S. and Kaiser, J. W.: Daily global fire radiative power fields estimation from one or two MODIS instruments, Atmos. Chem. Phys., 14, 13377–13390, doi:10.5194/acp-14-13377-2014, 2014.

Rissler, J., Vestin, A., Swietlicki, E., Fisch, G., Zhou, J., Artaxo, P., and Andreae, M. O.: Size distribution and hygroscopic properties of aerosol particles from dry-season biomass burning in Amazonia, Atmos. Chem. Phys., 6, 471–491, doi:10.5194/acp-6-471-2006, 2006.

Roberts, G. C. and Nenes, A.: A continuous-flow streamwise thermal-gradient CCN chamber for atmospheric measurements, Aerosol Sci. Tech., 39, 206–221, doi:10.1080/027868290913988, 2005.

Rose, D., Nowak, A., Achtert, P., Wiedensohler, A., Hu, M., Shao, M., Zhang, Y., Andreae, M. O., and Pöschl, U.: Cloud condensation nuclei in polluted air and biomass burning smoke near the mega-city Guangzhou, China – Part 1: Size-resolved measurements and implications for the modeling of aerosol particle hygroscopicity and CCN activity, Atmos. Chem. Phys., 10, 3365–3383, doi:10.5194/acp-10-3365-2010, 2010.

Sandradewi, J., Prevot, A. S. H., Szidat, S., Perron, N., Lanz, V. A., Weingartner, E., and Baltensperger, U.: Using aerosol light absorption measurements for the quantitative determination of wood burning and traffic emission contributions to particulate matter, Environ. Sci. Technol., 42, 3316–3323, 2008.

Sciare, J., Bardouki, H., Moulin, C., and Mihalopoulos, N.: Aerosol sources and their contribution to the chemical composition of aerosols in the Eastern Mediterranean Sea during summertime, Atmos. Chem. Phys., 3, 291–302, doi:10.5194/acp-3-291-2003, 2003.

ACPD
15, 21539–21582, 2015

Sciare, J., Oikonomou, K., Favez, O., Liakakou, E., Markaki, Z., Cachier, H., and Mihalopoulos, N.: Long-term measurements of carbonaceous aerosols in the Eastern Mediterranean: evidence of long-range transport of biomass burning, Atmos. Chem. Phys., 8, 5551–5563, doi:10.5194/acp-8-5551-2008, 2008.

Seinfeld, J. H. and Pandis, S. N.: Atmos. Chem. Phys.: from Air Pollution to Climate Change, 2nd edition, J. Wiley, New York, USA, 2006.

Spracklen, D. V., Carslaw, K. S., Pöschl, U., Rap, A., and Forster, P. M.: Global cloud condensation nuclei influenced by carbonaceous combustion aerosol, Atmos. Chem. Phys., 11, 9067–9087, doi:10.5194/acp-11-9067-2011, 2011.

Stolzenburg, M. R. and McMurry, P. H.: TDMAFIT User's Manual, Particle Technology Laboratory, Department of Mechanical Engineering, University of Minnesota, Minneapolis, MN, USA, 55455, 1988.

Stolzenburg, M. R. and McMurry, P. H.: An ultrafine aerosol Condensation Nucleus Counter, Aerosol Sci. Tech., 14, 48–65, 1991.

Wiedensohler, A., Birmili, W., Nowak, A., Sonntag, A., Weinhold, K., Merkel, M., Wehner, B., Tuch, T., Pfeifer, S., Fiebig, M., Fjäraa, A. M., Asmi, E., Sellegri, K., Depuy, R., Venzac, H., Villani, P., Laj, P., Aalto, P., Ogren, J. A., Swietlicki, E., Williams, P., Roldin, P., Quincey, P., Hüglin, C., Fierz-Schmidhauser, R., Gysel, M., Weingartner, E., Riccobono, F., Santos, S., Grüning, C., Faloon, K., Beddows, D., Harrison, R., Monahan, C., Jennings, S. G., O'Dowd, C. D., Marinoni, A., Horn, H.-G., Keck, L., Jiang, J., Scheckman, J., McMurry, P. H., Deng, Z., Zhao, C. S., Moerman, M., Henzing, B., de Leeuw, G., Löschau, G., and Bastian, S.: Mobility particle size spectrometers: harmonization of technical standards and data structure to facilitate high quality long-term observations of atmospheric particle number size distributions, Atmos. Meas. Tech., 5, 657–685, doi:10.5194/amt-5-657-2012, 2012.

Winker, D. M., Vaughan, M. A., Omar, A., Hu, Y., Powell, K. A., Liu, Z., Hunt, W. H., and Young, S. A.: Overview of the CALIPSO mission and CALIOP data processing algorithms, J. Atmos. Ocean. Tech., 26, 2310–2323, doi:10.1175/2009JTECHA1281.1, 2009.

ACPD
15, 21539–21582, 2015

Table 1. Calculated chemical dispersion in terms of $\sigma(\kappa)/\kappa$ for the four studied fire events and all measured particle sizes.

	60 nm	80 nm	100 nm	120 nm
Chios	0.85 ± 0.14	0.73 ± 0.14	0.60 ± 0.20	0.41 ± 0.16
Croatia	0.77 ± 0.18	0.68 ± 0.19	0.44 ± 0.12	0.41 ± 0.10
Euboea	0.70 ± 0.20	0.49 ± 0.10	0.32 ± 0.08	0.29 ± 0.06
Andros	0.71 ± 0.10	0.52 ± 0.13	0.34 ± 0.10	0.30 ± 0.06

ACPD
15, 21539–21582, 2015

Table 2. Average CFSTGC-derived κ_{CCN} values and HTDMA-derived κ_{HTDMA} values for the selected particles sizes.

	κ_{HTDMA}	κ_{CCN}
60 nm	0.23 ± 0.07	0.22 ± 0.05
80 nm	0.28 ± 0.1	0.39 ± 0.1
100 nm	0.3 ± 0.1	0.44 ± 0.1
120 nm	0.33 ± 0.11	0.49 ± 0.13

ACPD
15, 21539–21582, 2015

Table 3. Percentage of externally mixed samples (B_f), the hygroscopic parameter of the less and more hygroscopic mode (κ_1, κ_2), respectively, and the number fraction of particles residing in the less hygroscopic mode (N_{f1}) during the Chios event (20–21 August 2012).

d_p(nm)	Bf (%)	κ_1	N_{f1}	κ_2
60	6.9	0.05 ± 0.021	0.172 ± 0.063	0.182 ± 0.013
80	20.0	0.048 ± 0.021	0.33 ± 0.143	0.185 ± 0.032
100	23.0	0.058 ± 0.025	0.428 ± 0.236	0.21 ± 0.04
120	30.4	0.049 ± 0.025	0.465 ± 0.19	0.197 ± 0.04

ACPD
15, 21539–21582, 2015

Table 4. Same as Table 3, during the Euboea event (3–5 September 2012).

d_p(nm)	Bf (%)	κ_1	N_{f1}	κ_2
60	5.3	0.086 ± 0.071	0.372 ± 0.336	0.314 ± 0.192
80	15.2	0.061 ± 0.036	0.312 ± 0.174	0.197 ± 0.028
100	26.5	0.048 ± 0.026	0.387 ± 0.186	0.195 ± 0.033
120	28.2	0.047 ± 0.026	0.404 ± 0.191	0.191 ± 0.027

ACPD
15, 21539–21582, 2015

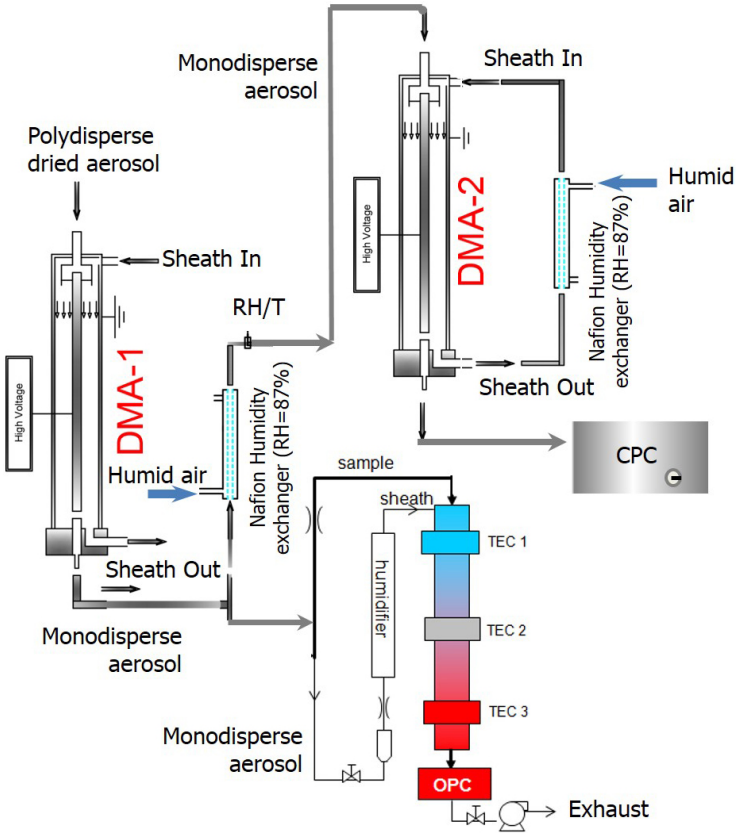

Figure 1. Schematic of the setup used for the CCN and mixing state measurements.

ACPD
15, 21539–21582, 2015

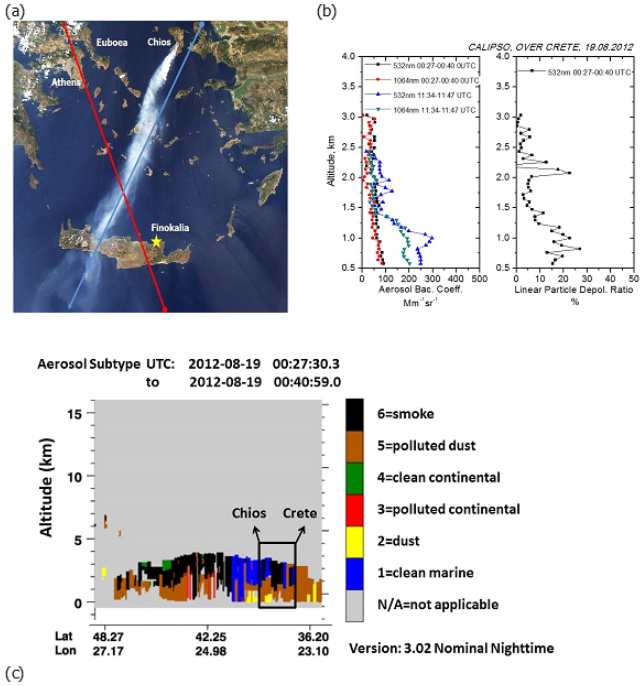

Figure 2. (a) Satellite composite view from MODIS of the fire plume emerging from the island of Chios on 18 August 2012 (courtesy on NASA). The blue and red lines delineate the two ground tracks of the CALIPSO satellite during its overpass over Crete on 19 August 2012 between 00:27–00:40 and 11:34–11:47 UTC, **(b)** Vertical profiles of the aerosol backscatter coefficient (in $km^{-1}\,sr^{-1}$) at 532 and 1064 nm (left) and linear particle depolarization ratio at 532 nm (right) measured by CALIPSO and **(c)** Vertical profiles of the aerosol subtypes captured by CALIPSO during its overpass over Crete; the marked area is located just at the NW of Finokalia station (00:27–00:40 UTC).

ACPD
15, 21539–21582, 2015

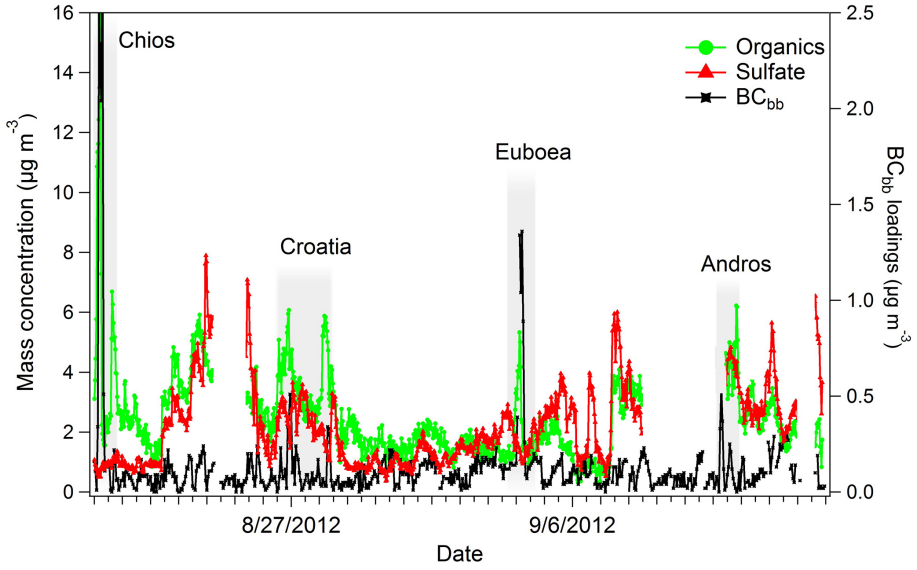

Figure 3. Time series concentrations of major PM_1 species that contribute in the identification of the BB events. The shaded areas represent the four considered fire events.

ACPD
15, 21539–21582, 2015

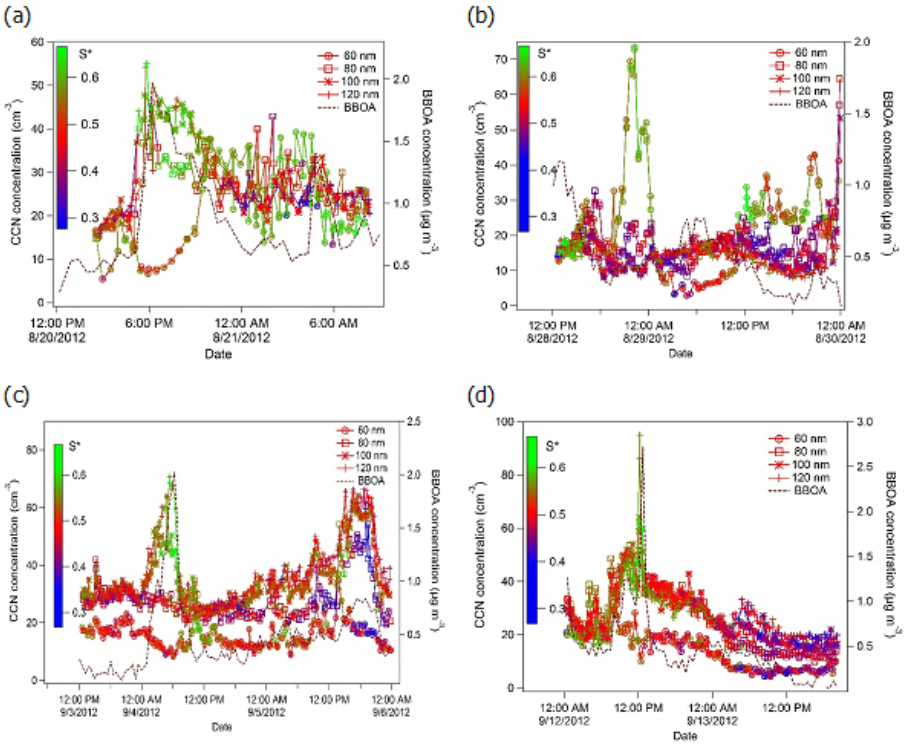

Figure 4. CCN concentrations for the selected particle sizes during the arrival of the smoke plumes for **(a)** Chios, **(b)** Croatia, **(c)** Euboea and **(d)** Andros. The black solid line represents the biomass burning component of the organic aerosol at the given time.

ACPD
15, 21539–21582, 2015

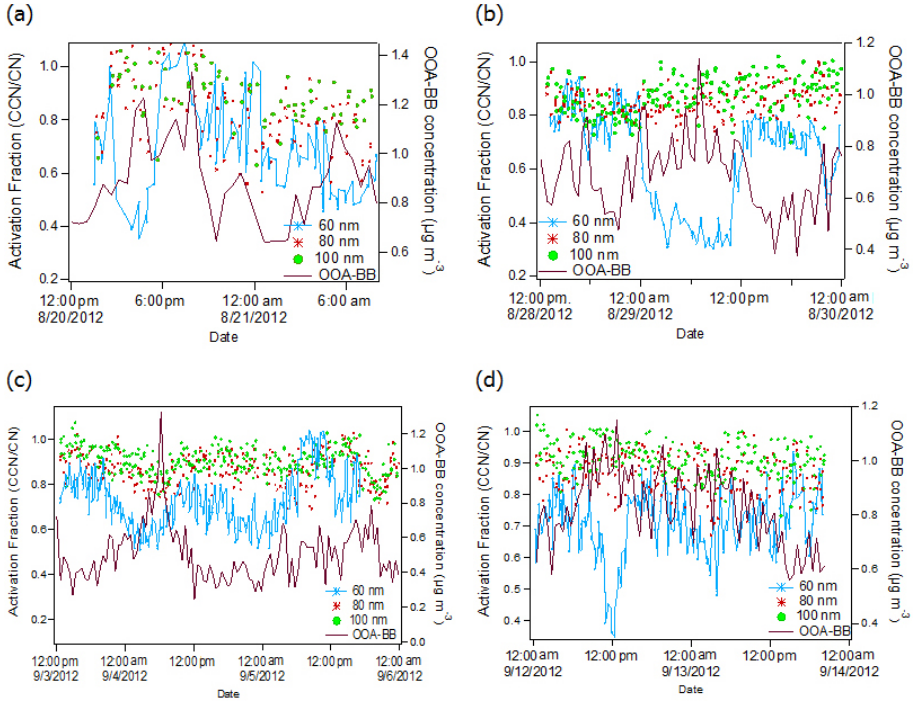

Figure 5. Activation fractions for the selected particle sizes during the arrival of the smoke plumes for **(a)** Chios, **(b)** Croatia, **(c)** Euboea and **(d)** Andros. The brown solid line represents the processed biomass burning component of the organic aerosol.

ACPD
15, 21539–21582, 2015

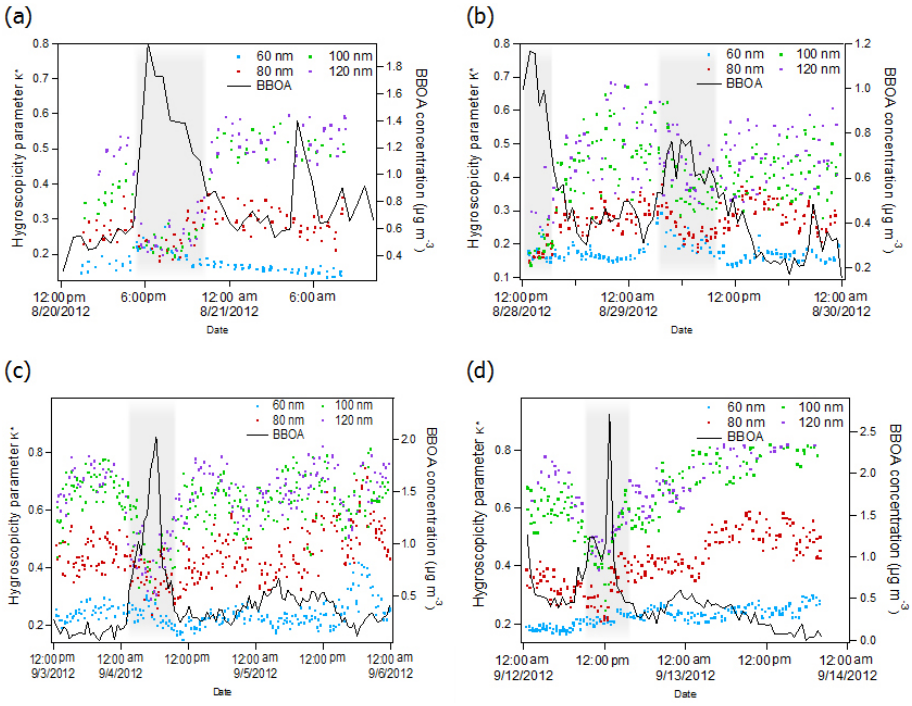

Figure 6. Characteristic hygroscopicity parameters of the selected particle sizes for **(a)** Chios, **(b)** Croatia, **(c)** Euboea and **(d)** Andros. The solid line represents the biomass burning component of the organic aerosol at the given time and circles represent the smoke plume arrival time. The shaded areas represent the smoke plume influence period.

ACPD
15, 21539–21582, 2015

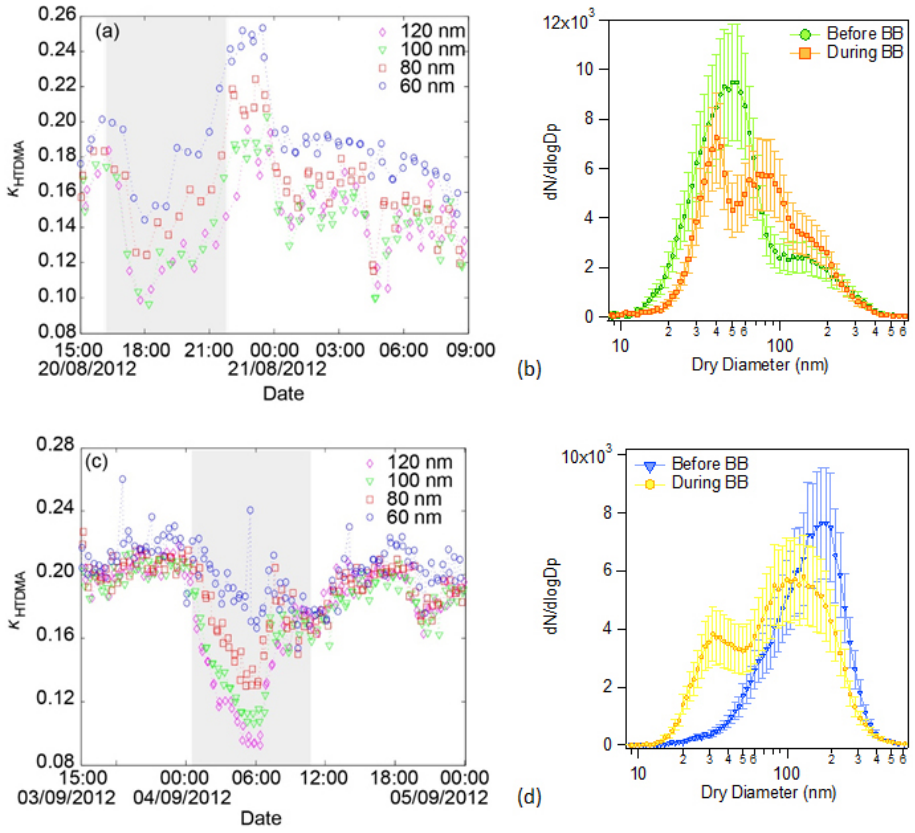

Figure 7. Cumulative growth factors from the HTDM **(a)** and **(c)** and number size distributions from the SMPS **(b)** and **(d)** for the Chios and Euboea fire events, respectively. The shaded areas represent the smoke plume influence period.

ACPD
15, 21539–21582, 2015

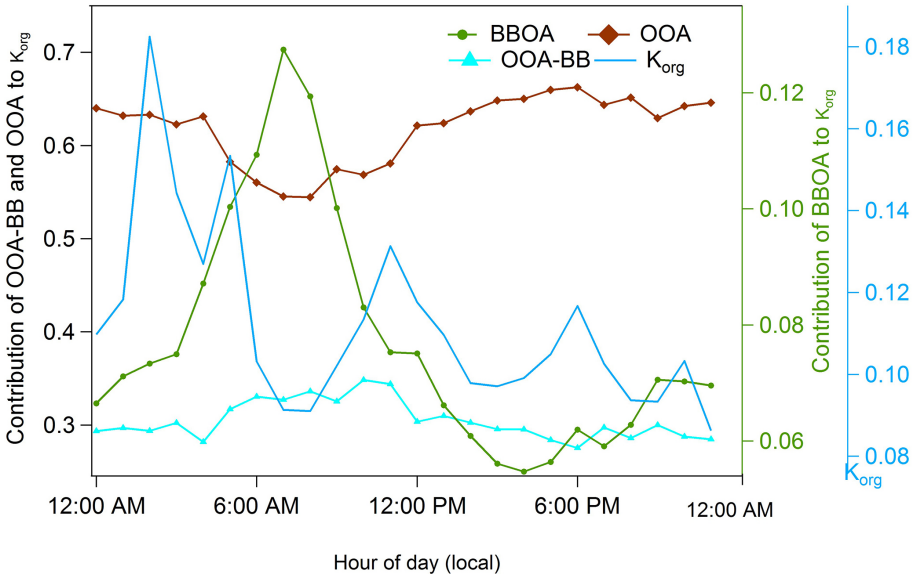

Figure 8. Average diurnal contribution of each organic aerosol factor to the κ_{org} computed by multiplying the mass fraction by the corresponding inferred hygroscopicity parameter and the predicted diurnal profile of the total κ_{org} in the ambient aerosol.

ACPD
15, 21539–21582, 2015